ADVANCED ENERGY MATERIALS
www.advenergymat.de

A Thin and Ultrahigh-Ionic-Conductivity Composite Electrolyte With 3D Aramid Nanofiber Networks Toward Ambient-Temperature Lithium Metal Batteries

Dongmei Zhang, Xianglong Meng, Wendi Zhang, Jinshan Mo, Qian Zhao, Baoyi Wang, Qianxiao Fan, Lehao Liu, Tianrong Yang, Yilong Jin, Rongmin Zhou, Mengxuan Zhang, and Meicheng Li**

The low ambient-temperature ionic conductivity and undesired compatibility with electrode materials are hindering the practical application of solid-state electrolytes in high-safety and high-energy-density lithium metal batteries. Herein, an ultrahigh ionic conductivity composite electrolyte is prepared by introducing a 3D aramid nanofiber (ANF) framework in succinonitrile (SN)-lithium bis (trifluoromethylsulphonyl) imide (LiTFSI) electrolytes. Theoretical calculations and experimental characterizations reveal that the ANF framework-based composite electrolyte (CPE) has dual fast-ion pathways: one Li^+ pathway along the 3D ANF frameworks with the coordination interaction between the amide groups and Li^+ (especially Li^+ pathway between SN and ANF), and another Li^+ pathway along the SN molecules in the form of $Li(SN)_x^+$ cluster. Meanwhile, the hydrogen bonding interaction between the –NH groups of the ANF and the cyano groups of SN captures the free SN molecules, improving the chemical compatibility with Li metal. The well-designed CPE membrane with a small thickness of 24 µm exhibits a high Li^+ conductivity of 1.69×10^{-3} S cm^{-1}. Notably, the Li|CPE|$LiFePO_4$ cell shows a long cycle life at 30 °C (0.5 C, >300 cycles, a capacity retention of 94.3%). The all-solid-state Li||$LiNi_{0.5}Co_{0.2}Mn_{0.3}O_2$ battery with an ultrahigh active mass loading of 20 mg cm^{-2} also displays excellent cycle performance.

1. Introduction

Lithium-ion batteries are used in a few important fields including transportation, grid storage, and residential backup power.[1–4] However, the safety risks triggered by the flammable liquid electrolytes hinder further commercial applications of lithium-ion batteries. All-solid-state lithium metal batteries by replacing the flammable liquid electrolytes with solid-state electrolytes are considered a promising electrochemical energy storage device to meet the ever-increasing requirements for high energy density and high safety.[5–6] SSEs are commonly divided into inorganic electrolytes and polymer electrolytes. Inorganic electrolytes usually have high ionic conductivity at ambient temperature, wide electrochemical windows, and fabulous chemical stability to lithium metals, while they suffer from high resistance at the electrode/electrolyte interfaces because of the poor solid/solid contact, severely limiting their practical application.[7–8] In addition, the thickness of the inorganic solid-state electrolyte pellets is large (usually several hundred micrometers), which results in the increase of the resistance and the decrease of the energy density of the solid-state batteries.[8–12] Compared with the inorganic electrolyte counterparts, solid polymer electrolytes have attracted much attention by virtue of light weight, flexibility, good processability, low electrolyte/electrode interface resistance, and low price.[2,13–18] However, the application of solid polymer electrolytes is greatly hindered by insufficient ionic conductivity at room temperature, mechanical strength, and lithium dendrite inhibition ability.[19] Thus, it is of significance to develop thin electrolyte membranes with high ionic conductivity and good compatibility with lithium metal toward room-temperature solid-state metallic lithium batteries for their practical application.

Solution infusion is considered as one of the most important routes to prepare thin solid-state composite electrolyte (CPE) membranes by infusing the electrolyte solution/slurry into porous substrates and then evaporating the solvents.[20–23] The ionic conductivity of the CPE films is greatly affected by the electrolyte matrices, while the thickness mainly relies on the porous substrates.[21,24–26] The CPE membranes with porous ceramic electrolyte substrates exhibit high ionic conductivity[27]; however, these CPE membranes are brittle, and the thickness is commonly higher than 100 µm. To reduce the thickness,

D. Zhang, X. Meng, W. Zhang, J. Mo, Q. Zhao, B. Wang, Q. Fan, L. Liu, T. Yang, Y. Jin, R. Zhou, M. Zhang, M. Li
State Key Laboratory of Alternate Electrical Power System with Renewable Energy Sources
School of New Energy
North China Electric Power University
Beijing 102206, China
E-mail: lehaoliu@ncepu.edu.cn; mcli@ncepu.edu.cn

The ORCID identification number(s) for the author(s) of this article can be found under https://doi.org/10.1002/aenm.202403565

DOI: 10.1002/aenm.202403565

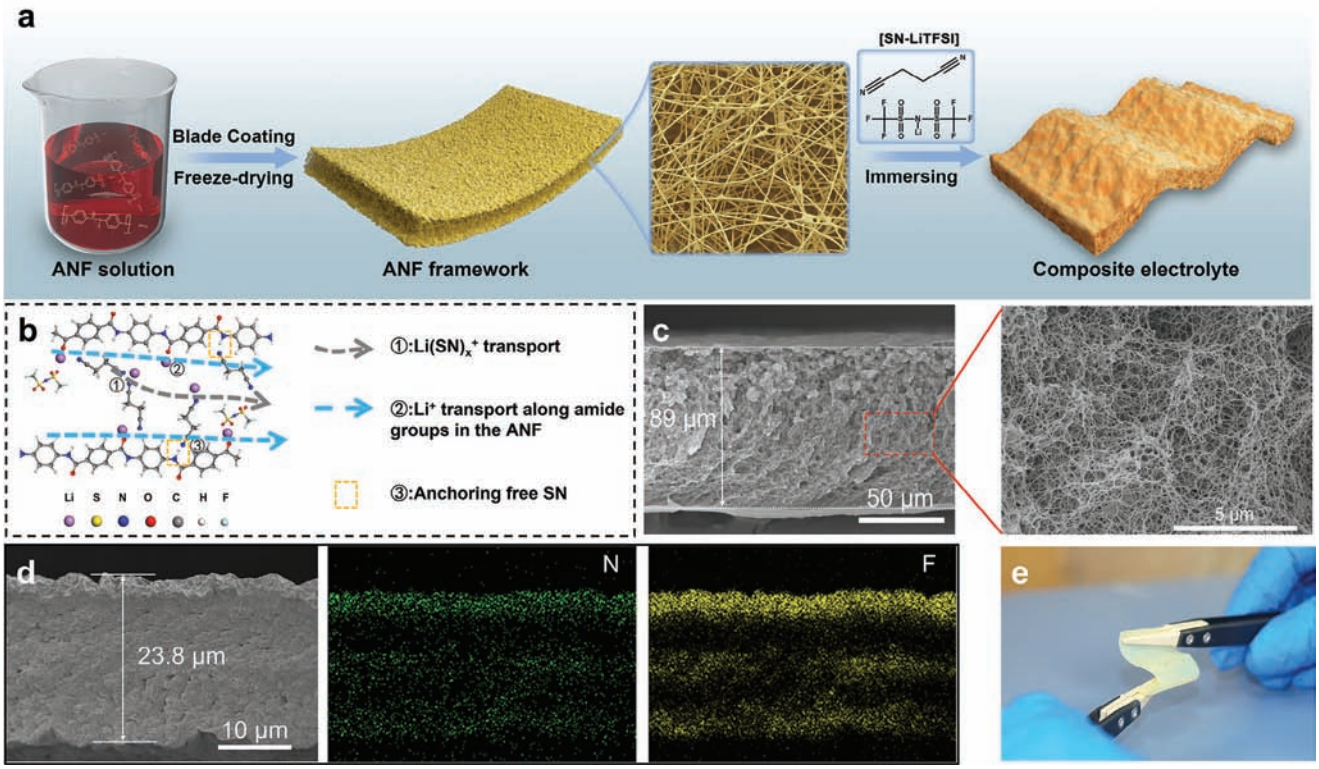

Figure 1. Schematic diagram of the preparation process and characterization of the composite electrolyte membranes. a) Schematic illustration of the preparation of the composite electrolyte membranes by a solution infusion method. b) Schematic illustration of the interaction between the amide groups in the ANF and SN-LiTFSI electrolyte matrix for facilitating Li^+ conduction and anchoring free SN molecules. c) Cross-sectional SEM images of the ANF framework films and d) the composite electrolyte membranes with the corresponding EDS element mappings of the N and F elements. e) Optical photograph of the composite electrolyte membranes with high flexibility.

porous organic skeletons such as nonwoven fabrics, polyimide nanofibers, and polyethylene separators are further utilized to prepare CPE membranes.[24,26,28–30] Nevertheless, the organic substrates do not provide rapid Li^+ transport pathways, decreasing the overall ionic conductivity of the CPE films. Thus, it is necessary to develop a high-strength organic substrate with continuous Li^+ transport pathways to increase the ionic conductivity of the thin CPE films.

Aramid nanofibers (ANFs) with abundant polar amide groups, large aspect ratios, high mechanical strength, and low electroconductivity have been used as multifunctional nanofillers to improve the electrical and mechanical properties of the solid polymer electrolytes.[31–34] In this work, we prepare a thin, ultrahigh ionic conductivity CPE membrane by filling succinonitrile (SN)-lithium bis(trifluoromethyl sulphonyl) imide (LiTFSI) electrolytes in 3D porous ANF framework films via a facile and scalable solution infusion method (**Figure 1a**). The introduction of the ANF frameworks effectively reduces the crystallization of the electrolyte matrix, accelerating the Li^+ transport in the electrolyte matrix. Apart from the fast-ion pathways in the SN-LiTFSI phase, the 3D continuous ANF networks with abundant amide groups coordinate with Li^+ and function as additional fast-ion pathways, thus greatly improving the ambient-temperature ionic conductivity (1.67×10^{-3} S cm^{-1}) and Li^+ transference number (0.57). In addition, the coordination interaction between the –N–H groups of the ANF and the –C≡N groups of the SN prevents the side reactions between the lithium metal and SN by capturing SN molecules to restrict their movement toward the lithium electrodes (Figure 1b). Therefore, the CPE-based Li||$LiFePO_4$ and Li||$LiNi_{0.5}Co_{0.2}Mn_{0.3}O_2$ cells with an ultrahigh active mass loading exhibit excellent cycling stability and rate performance at room temperature. This work offers a facile and scalable method to prepare thin, ultrahigh-conductivity electrolyte membranes with a 3D multifunctional framework structure for their practical application in solid-state metallic lithium batteries.

2. Results and Discussion

2.1. Preparation of the Composite Electrolyte Membranes

The schematic preparation process of the porous ANF framework films and the CPE membranes is shown in Figure 1a. First, we prepared the ANF solution by dispersing the aramid microfibers in dimethyl sulfoxide (DMSO) with the deprotonation of the ANFs (Figure S1, Supporting Information). The solution was then deposited on glass slides via a blade-coating method, and the thickness of the coating layers was controllable by adjusting the gap of the scraper. After that, the ANF coating layers were immersed in deionized water to protonate ANF for forming 3D continuous ANF frameworks by hydrogen bonding between the amide groups and then put into a mixture of deionized water and *tert*-butyl alcohol for easy freezing of the solution.[35] Finally, the

3D porous ANF films (thickness of 89 µm) were prepared by the freeze-drying process (Figure 1c). The cross-sectional SEM images of the ANF framework films revealed the 3D interconnected pore structure. The nitrogen adsorption-description isotherm further demonstrated that the ANF films had a large number of pores. The ANF framework films exhibited a type IV adsorption-description isotherm with a mixed hysteresis loop of H2 and H3, indicating the existence of micropores, mesopores, and macropores. The corresponding inset in Figure S2 (Supporting Information) also confirmed that the pore size distribution followed the Barrett-Joyner Halenda (BJH) model. The average diameter of the pores was 51.3 nm (pore diameter range from 44.2 to 67.6 nm) and 76.0 nm (pore diameter range from 67.6 to 91.6 nm). The proper pore size of the ANF framework films was helpful for the electrolyte matrix filling without degrading the mechanical strength.

In this work, the SN-LiTFSI electrolyte matrix was prepared by mixing SN and LiTFSI with a molar ratio of 20:1 to guarantee high ionic conductivity (Figure S3, Supporting Information).[20] After that, the molten SN-LiTFSI electrolyte was filled in the porous ANF framework films to obtain the CPE membranes in a vacuum condition (Figure 1a). After the solution immersing process, the color of the films changed from bright yellow to dark yellow (Figure S4, Supporting Information). As shown in Figure S5 (Supporting Information), the porous ANF framework films were completely filled with the SN-LiTFSI matrix without any obvious pores on the surface. The CPE membranes had a high content of the SN-LiTFSI matrix (≈94.4 wt.%) (Tables S1, andS2, Supporting Information). Meanwhile, the cross-section SEM images and the corresponding energy-dispersive spectral (EDS) mapping images of the CPE membranes further verified that the SN-LiTFSI matrix was completely filled in the ANF frameworks (Figure 1d), and the thickness of the CPE membranes was 24 µm (≈1/4 of the thickness of the porous ANF framework films) due to the deformation of the flexible porous ANF films during the filling and drying processes. Besides, the CPE membranes with the 3D continuous ANF frameworks also had high flexibility, and thus the membranes can be folded and unfolded many times without fracture (Figure 1e).

2.2. Electrochemical, Mechanical, and Thermal Properties of the Electrolytes

The ionic conductivities of various electrolytes at temperatures ranging from 30 to 80 °C are shown in **Figure 2a**. The curve characteristic of CPE showed a slight inflection point (50–80 °C) above the melting temperature of the SN (>50 °C), which could be attributed to the change in the state of SN.[36–37] The SN in plastic crystal state was fully filled in the pores of the ANF frameworks at room temperature, but the molten SN-LiTFSI can easily move in the CPE and the ion transport pathways in the SN-LiTFSI matrices became incontinuous, resulting in the decrease of the ionic conductivity at 60 °C. However, the 3D ANF frameworks in the CPE can anchor the molten SN to prevent further movement and the leakage of the SN-LiTFSI matrices, because of the hydrogen bonding between the amide groups and the cyano groups. Thus, the ionic conductivity of the CPE increased again at higher temperatures.[27,38] The CPE membranes also exhibited an ultra-high ionic conductivity of 1.69×10^{-3} S cm^{-1} at 30 °C, which was 3 orders of magnitude higher than the traditional polyethylene oxide (PEO)-based electrolytes (5.35×10^{-6} S cm^{-1}) (Table S3, Supporting Information). The effect of the porous ANF frameworks on the ionic conductivity of the CPE membranes was investigated by X-ray diffraction (XRD) patterns (Figure 2b). There were no obvious characteristic peaks of SN (≈19° and 29°) in the curve of the CPE electrolyte, meaning that the whole SN-based electrolyte matrix was mostly amorphous. The decrease in crystallinity indicated an accelerated SN molecules isomer transition rate from gauche to trans and an increased defect density, which could facilitate Li^+ transport and enhance the ionic conductivity. Differential scanning calorimetry (DSC) measurements also revealed the roles of the porous ANF frameworks in the CPE membranes. There were two endothermic peaks at −37.4 and 39.2 °C in the curve of the SN-LiTFSI electrolytes, corresponding to the transition temperature (T_{cp}) from normal crystal to plastic crystal phase and the melting point (T_m), respectively (Figure 2c). In the CPE membranes, the T_m peak almost disappeared, again demonstrating that the crystallinity of SN was effectively reduced. In addition, the T_{cp} was also found to occur at −37.2 °C, indicating that the addition of the ANF frameworks showed little effect on this transition peak. These test results further implied that the crystallization of SN in the CPE membranes at low temperatures was restrained due to the potential interaction between the SN-LiTFSI electrolyte matrix and the ANF frameworks.

The Li^+ transference number (t_{Li+}) of the electrolytes is also a crucial factor in evaluating the mobility of Li^+ and is measured with the combination of chronoamperometry (CA) and electrochemical impedance spectroscopy (EIS). Due to the interaction between the $TFSI^-$ anions and the amide groups of the ANFs, the mobility of the anions was limited and the CPE membranes delivered a higher Li^+ transference number of 0.57 than the SN-LiTFSI/glass fiber composite electrolyte (denoted as Glass fiber, 0.34) and the conventional PEO-based polymer electrolyte (0.22, Figure 2d; Figure S6, Supporting Information).[31] These results illustrated that the ANF frameworks could promote to release of more Li^+ from LiTFSI and improve the Li^+ conduction. This would be beneficial to reduce the electrode polarization and prevent the lithium dendrite growth.[39–40] To investigate the electrochemical stability of electrolyte membranes, the linear sweep voltammetry (LSV) measurement is employed. Compared to the PEO-based electrolyte (3.2 V vs Li/Li^+), the sweep range of the CPE and SN-LiTFSI/glass fiber composite electrolyte was extended to 5.0 and 4.9 V without any obvious current peaks, respectively. Thus, the CPE membranes can be compatible with high-voltage cathode materials for high-energy-density batteries (Figure 2e; Figure S7, Supporting Information).

Because of the introduction of the 3D porous ANF framework films with a high tensile strength of 2.1 MPa (Figure S8, Supporting Information), the mechanical strength of the CPE was significantly improved. The CPE displayed a higher ultimate tensile stress of 1.3 MPa than the SN-LiTFSI/glass fiber composite electrolyte (0.1 MPa) and the conventional PEO-based electrolyte (0.4 MPa) (Figure 2f; Figure S9, Supporting Information). Besides, the tensile strain of the CPE achieved 58% with the filling of the SN-based electrolyte matrix, which was 64 times that of the ANF films (0.9%). Thus, the CPE can achieve a combination of

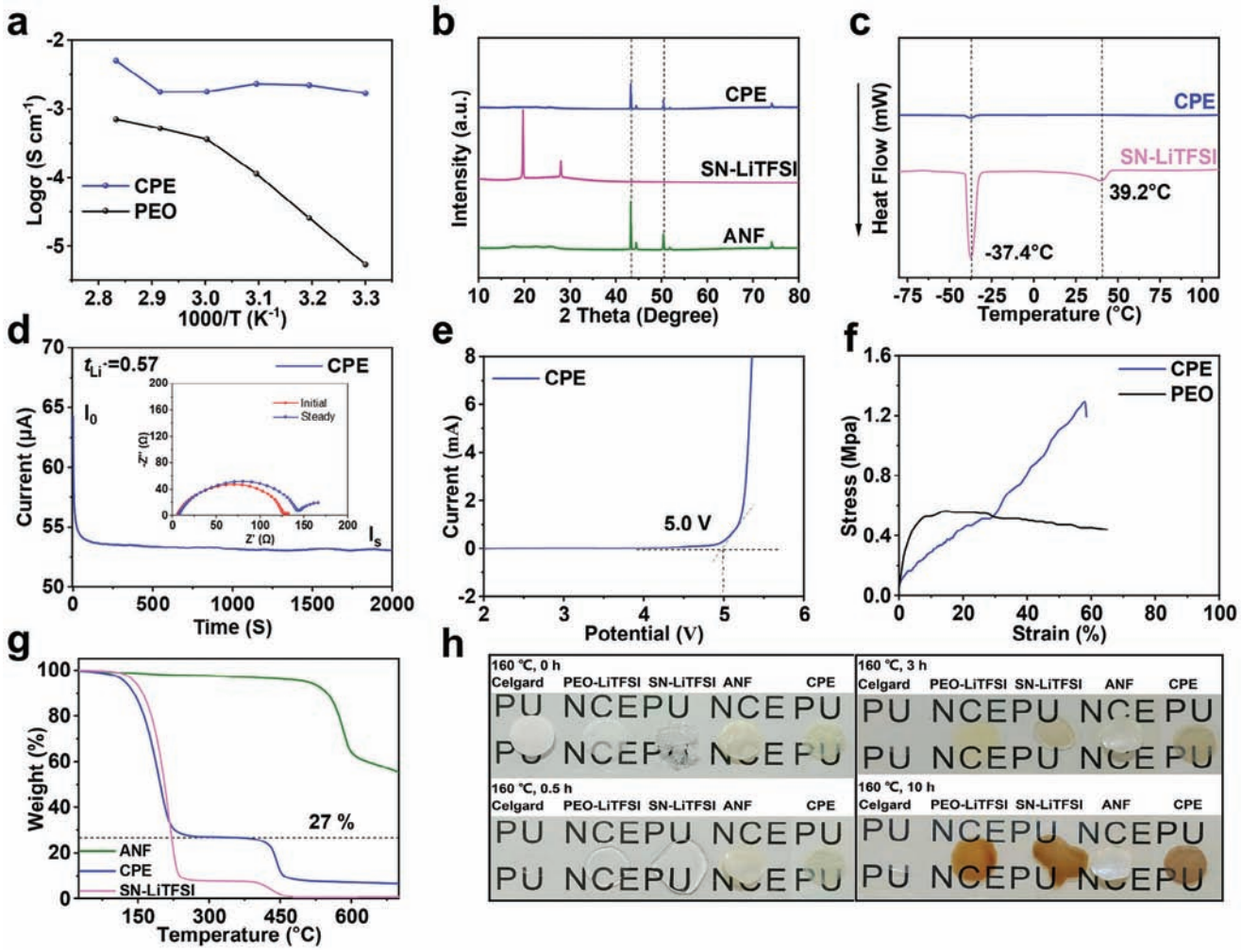

Figure 2. The performance of the composite electrolytes. a) Ionic conductivity of the electrolytes. b) XRD patterns of the ANF frameworks film, SN-LiTFSI electrolyte, and composite electrolyte. c) DSC curves of the SN-LiTFSI electrolyte and composite electrolyte. d) The chronoamperometry (CA) curve for the composite electrolyte at 30 °C at 0.01 V (The inset was the EIS Nyquist chart before and after the polarization). e) Liner sweep voltammetry (LSV) curves of composite electrolyte. f) Mechanical tensile stress-strain curves of the electrolytes. g) TGA curves of the ANF frameworks film, SN-LiTFSI electrolyte, and composite electrolyte. h) Optical photos at 160 °C for various hours in an oven of the electrolytes.

high mechanical strength and good flexibility, which is beneficial for suppressing lithium dendrite growth.[15,32,41–43]

As observed by the thermogravimetric analysis (TGA) in Figure 2g, the CPE exhibited 2 distinct stages of the degradation. The first stage, occurring ≈200 °C, corresponded to the decomposition of the SN. The second stage in the TGA curves at 452 °C represented the decomposition of LiTFSI. Specifically, the LiTFSI in the CPE showed enhanced thermal stability in comparison with the SN-LiTFSI electrolytes (≈432 °C). Meanwhile, it was noticed that a weight retention of ≈27% stabilized in the temperature range of 243–473 °C, indicating that the CPE had excellent thermal protection benefiting from the ANF frameworks (Figure 2g). The curve of the ANF films showed a significant weight loss at above 500 °C, indicating the degradation of the CO-NH and aromatic-NH bonds with subsequent decarboxylation of carbonyl end groups.[44–45] However, the CPE still displayed extraordinary thermal stability without weight loss over 500 °C, which should be attributed to the hydrogen bond interaction between the amide groups of the ANF and the cyano groups of the SN-based electrolyte matrix. Similarly, the thermal shrinkage behavior test was also carried out to investigate the superior thermostability of the CPE (Figure 2h). After storage at 160 °C in the air for 0.5 h, the commercial separator, and the PEO-based electrolyte samples exhibited visible shrinkage, while the CPE remained integrated, and its diameter change was almost negligible even after 3 h. The TGA measurements and thermal shrinkage behavior tests demonstrated that the CPE possessed excellent thermal stability, which can be attributed to the good thermal properties of the ANF frameworks and the interaction between the ANF frameworks and the SN-LiTFSI matrix.

2.3. Effect of the ANF Frameworks on the CPE

Both theoretical calculations and experimental characterizations were combined to investigate the effect of the ANF frameworks

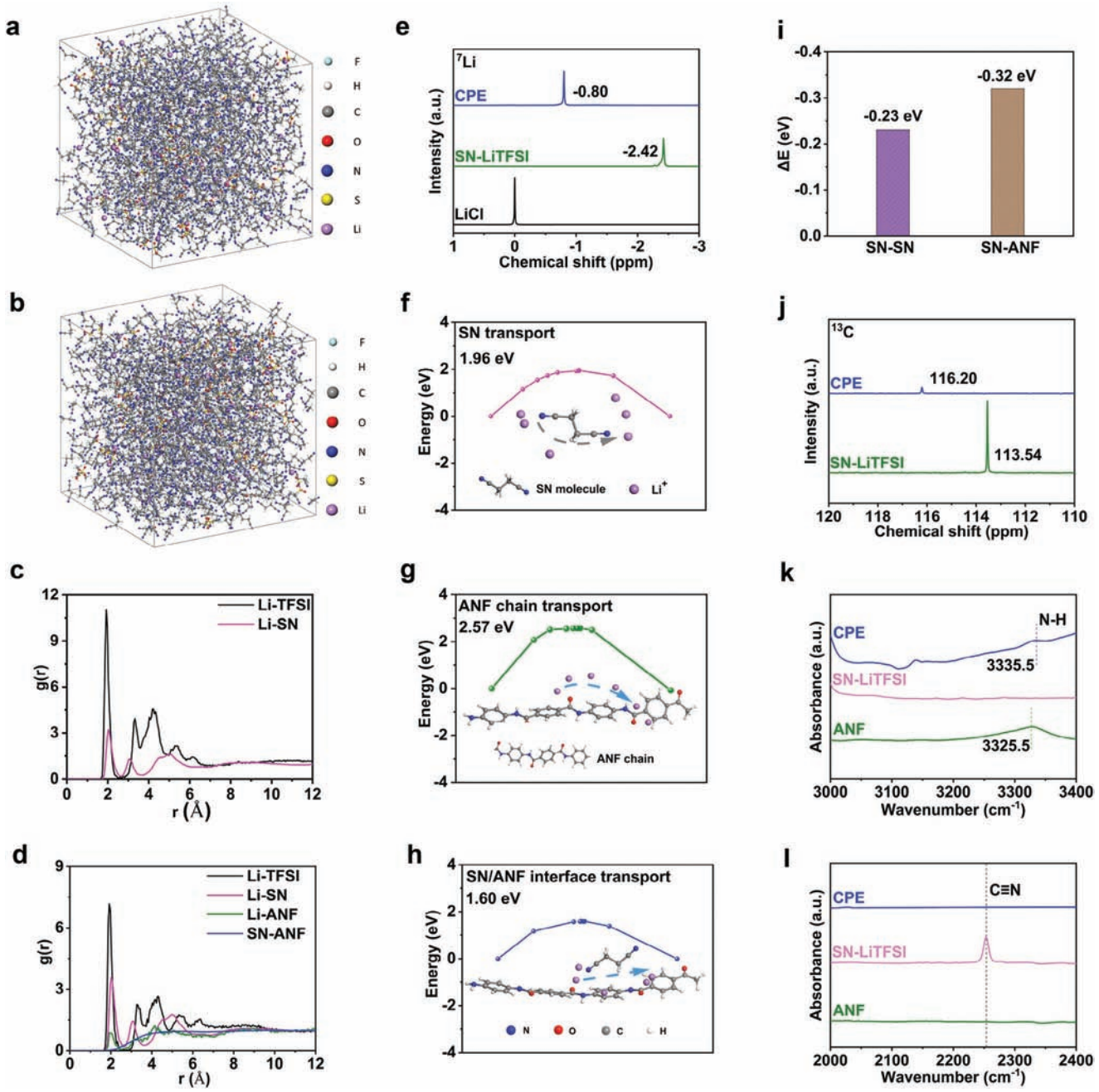

Figure 3. The understanding of the roles of the ANF frameworks. Snapshots based on MD simulation of a) SN-LiTFSI electrolyte and b) composite electrolyte system. Radial distribution functions g(r) of Li–TFSI, Li–SN, Li–ANF, and SN–ANF pairs calculated from MD simulation trajectories at 303 K for c) SN-LiTFSI electrolyte and d) composite electrolyte. e) ^{7}Li-NMR spectra of SN-LiTFSI electrolyte and composite electrolyte. Li^+ migration energy barriers of f) the SN transport, g) the ANF chain transport, and h) the SN/ANF interface transport. i) The binding energy of SN–SN and SN–ANF. j) ^{13}C-NMR spectra of SN-LiTFSI electrolyte and composite electrolyte. k, l) FTIR spectra of ANF framework film, SN-LiTFSI electrolyte, and composite electrolyte.

on the CPE. The representative snapshots of the SN-LiTFSI electrolytes and the CPE showed that the ions were uniformly distributed throughout the electrolytes from molecular dynamic (MD) simulations (**Figure** 3a,b). In the SN-LiTFSI electrolyte and the CPE, the SN molecules and Li^+ formed a solvated sheath-like structure due to the intermolecular interaction between SN and LiTFSI (Figure S10, Supporting Information). That is, the SN molecules serve as Li^+ acceptors, resulting in a Li^+ pathway along the SN molecules in the form of the solvated $Li(SN)_x^+$ clusters.[2,46] Meanwhile, according to the calculated radial distribution function, the sharp peak of Li–SN (2.0 Å) still maintained consistent values even in the CPE, again verifying that Li^+ can be transported in the form of the solvated molecules clusters (i.e., $Li(SN)_x^+$) in the CPE (Figure 3c,d). Compared to the

SN-LiTFSI, the iconic snapshots of the CPE based on MD simulations also revealed another coordination environment of Li^+ (Figure S10b, Supporting Information). The ANF chains with abundant lithiophilic polar functional groups (i.e., amide groups) can easily interact with Li^+. In Figure 3d, the dominant peak intensity of Li-TFSI at 1.9 Å displayed an obvious decline, indicating that there was an interaction between the ANF and LiTFSI after the introduction of the ANF, which could facilitate the dissociation of LiTFSI to release more Li^+. Moreover, the peak at 1.9 Å related to the coordination of Li–ANF appeared clearly, which also proved that the ANF chains can easily coordinate Li^+ and participate in the Li^+ transport. In addition, nuclear magnetic resonance (NMR) measurements were carried out to illustrate the Li^+ transport mechanism. The ^{7}Li NMR spectra are shown in Figure 3e. The ^{7}Li chemical signals shifted from –2.42 ppm to –0.80 ppm after the introduction of the ANF frameworks, indicating weakened Li–TFSI interactions, strengthened Li–SN coordination, and the existence of Li–ANF coordination.[47–48]

To further demonstrate the migration pathways of lithium ions in the CPE, the migration energy barrier of Li^+ was calculated according to DFT calculation (Figure 3f–h). The migration energy barrier of Li^+ along the ANF chains was 2.57 eV, which was higher than that of Li^+ along SN molecules (1.96 eV). However, the migration energy barrier of Li^+ between the ANF chains and the SN molecules (1.60 eV) was much lower than that of Li^+ along the ANF chains, implying that the SN molecules and the ANF chains with a large number of lithium coordination sites jointly contributed to the Li^+ conduction at the SN/ANF interfaces. The abovementioned results illustrated that the CPE had dual fast-ion pathways, i.e., one pathway along the SN molecules through the $Li(SN)_x^+$ clusters and another one along the amide groups of the ANF chains (especially the Li^+ pathway between the ANF and the SN), together contributing to the high ionic conductivity of the CPE at room temperature (1.69×10^{-3} S cm^{-1}).

Meanwhile, we can see a noticeable SN–ANF pair peak at ≈5.0 Å, which was smaller than the distance between —C≡N and —C≡N (≈7.0 Å) in the SN, implying a strong interaction between the SN and the ANF (Figure 3d). Density functional theory (DFT) calculations were also applied to obtain the binding energy of the geometric configuration-optimized systems (Figure 3i). The binding energy between the SN and the ANF was –0.32 eV, which was higher than that of the SN and the SN (–0.23 eV), again verifying that the SN was more likely to bind with the ANF rather than with itself by the dipole-dipole interaction. This anchoring of the SN molecules on the ANF frameworks would be helpful for inhibiting the free SN molecule migration and preventing the side reactions between SN and lithium metal.

To elaborate the interaction between SN and ANF frameworks deeply, ^{13}C NMR spectroscopy measurements and Fourier transform infrared (FTIR) were also carried out. The ^{13}C NMR peak of –C≡N in SN presented a significant displacement from 113.54 to 116.20 ppm in the CPE, suggesting that the electron cloud density ≈C≡N decreased and the coordination interaction between the SN and the ANF was likely to be formed (Figure 3j). Furthermore, the –C≡N peak of SN at 2254 cm^{-1} disappeared and the peak location of $–CH_2–$ in SN delivered a slight shift from 1424.7 to 1426.6 cm^{-1} when introducing the ANF frameworks (Figure 3k,l; Figure S11, Supporting Information). Simultaneously, the typical N–H characteristic peak in the ANF exhibited an apparent shift from 3325.5 to 3335.5 cm^{-1}. However, the –C—O peak of the ANF showed a nonobvious change. These results of the functional group's peak shift indicated that there was a hydrogen bond interaction between the –C≡N groups of the SN and the N–H groups of the ANF. These FTIR and NMR results also agreed well with the abovementioned MD simulation and DFT calculation analyses. In short, the ANF frameworks in the CPE can effectively anchor the SN molecules by the hydrogen bond interaction between the –C≡N groups of the SN and the N–H groups of the ANF, which is beneficial to prevent the movement of the SN molecules toward the lithium electrodes and improve the electrochemical compatibility between the CPE and the lithium metal electrodes.

2.4. Interfacial Resistance Against Li Dendrites

Benefiting from the high ionic conductivity, t_{Li^+}, and mechanical strength, the CPE is expected to provide excellent dynamic electrochemical stability and interfacial stability toward lithium metal. The symmetric Li||Li cells with the solid-state electrolytes were measured by galvanostatic cycling tests to further prove the superiority of the CPE. The interfacial affinity between the electrolytes and Li metals was first detected by EIS spectra (Figures S12 and S13, Supporting Information). The interfacial resistance of the Li|CPE|Li cell was 200 Ω, which was much lower than those of the Li|Glass fiber|Li (310 Ω) and the Li|PEO|Li (1610 Ω) cells. The smaller value for the CPE-based cells demonstrated the easier lithium ion migration between the electrolyte and the lithium electrodes.[49–50] In **Figure 4a**, the symmetric Li||Li cell with the PEO-based electrolyte delivered a high initial overpotential of 463 mV. And the cell suffered a rapid voltage increase after only over 42 h. The Li|Glass fiber|Li cell displayed a low initial overpotential of 34 mV. With the increase of the cycling time, the overpotential of the cell also increased. After 300 h, the voltage of the cell rapidly increased to 500 mV (Figure S14a, Supporting Information). In stark contrast, the Li|CPE|Li cell was stable even after over 600 h cycling with a lower overpotential of 25 mV under a current density of 0.1 mA cm^{-2} at 30 °C. Furthermore, a series of detailed curves of the Li|CPE|Li cells at 0–25, 260–280, and 500–520 h were smooth, which indicated that the CPE provided excellent dynamic electrochemical stability toward lithium metal. The critical current density (CCD) of the various electrolyte-based Li||Li cells was also tested (Figure 4b). The Li|PEO|Li and the Li|Glass fiber|Li cells showed low CCDs of 0.05 and 0.3 mA cm^{-2}, respectively (Figures S14b and S15, Supporting Information). In sharp contrast, the Li|CPE|Li cell exhibited better dynamic electrochemical stability and the corresponding charge/discharge overpotential profiles increased almost linearly when the current density increased from 0.05 to 0.5 mA cm^{-2} (Figure 4b). The improved interfacial property highlighted the high lithium ion transfer ability and good interface compatibility with Li metal, demonstrating the splendid interface stability and fast dynamics of the CPE.

To further investigate the dendrite inhibition ability of the composite electrolytes, SEM and X-ray photoelectron spectroscopy (XPS) measurements were conducted on the cycled lithium metal surfaces. After cycling for 200 h, plenty of Li dendrites and cracks appeared on the Li electrodes in the Li|PEO|Li

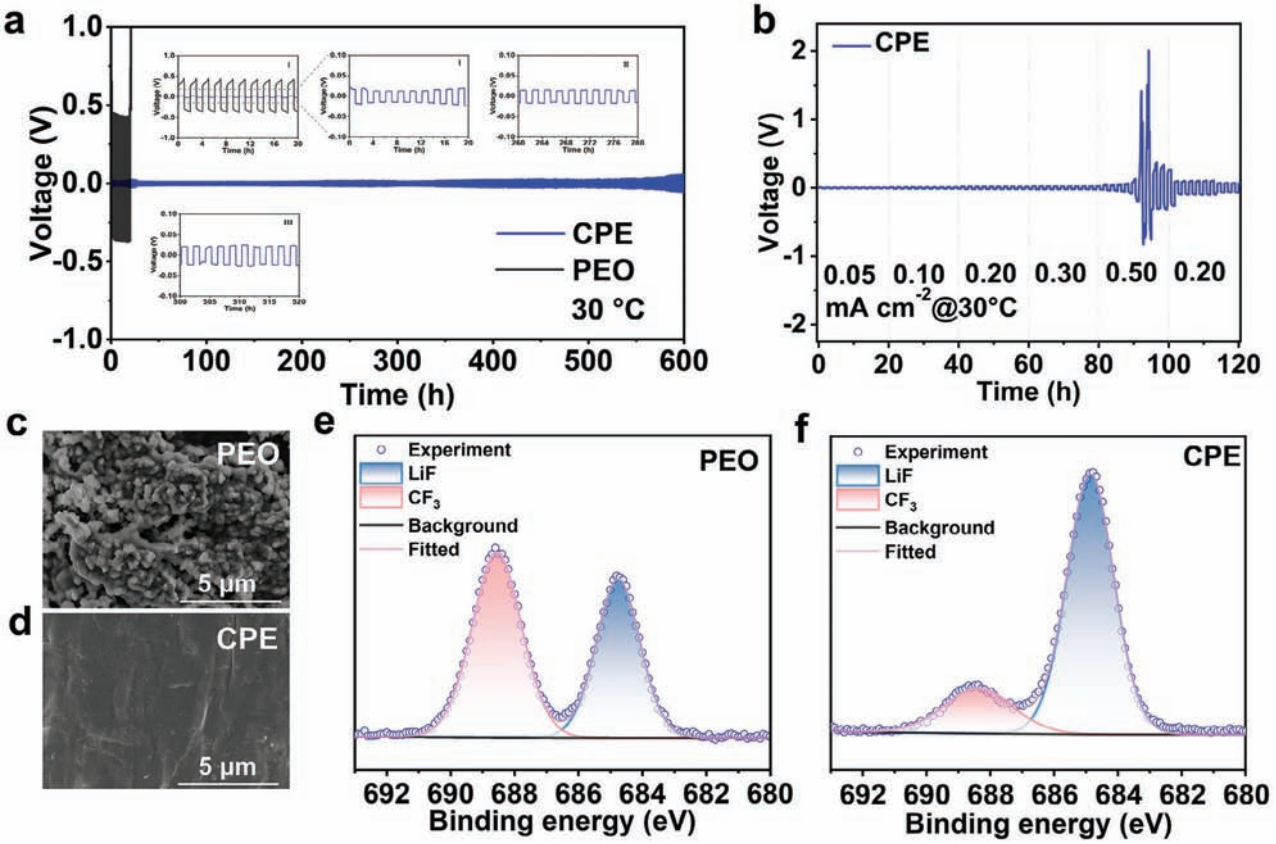

Figure 4. The Li||Li symmetrical cell performance. a) Long-term plating/stripping curves of the Li|CPE|Li cell and Li|PEO|Li cell at 0.1 mA cm^{-2}. The inset showed the voltage-time profiles of symmetric Li||Li cells in the cycling interval of (I) 0 to 20 h, (II) 260 to 280 h, and (III) 500 to 520 h. b) Critical current density test of the Li|CPE|Li cell from 0.05 to 0.5 mA cm^{-2}. Surface morphologies of the cycled Li anodes in c) Li|PEO|Li cell and d) Li|CPE|Li cell. XPS spectra of the cycled Li anodes from the symmetric battery using e) PEO-based electrolyte and f) composite electrolyte.

cell (Figure 4c). However, the lithium metal from the Li|CPE|Li cell maintained smooth and flat without any obvious lithium dendrites (Figure 4d). The F 1s XPS spectra of the cycled lithium metal are shown in Figure 4f. There was an obvious LiF peak that emerged for the cycled lithium metal from the Li|CPE|Li cell, whereas the CF_3 was the main content of the Li electrodes from the Li|PEO|Li cell (Figure 4e). The LiF-rich interface layers can effectively accelerate Li^+ transport and block electron migration during the plating and stripping process.[51–52] SEM images were also taken to detect the surficial microstructure change of the electrolyte membranes. A lot of Li deposition-resulted microparticles and large protrusions formed on the surface of the PEO-based electrolyte membranes. In stark contrast, there were no large protrusions on the surface of the CPE membranes (Figure S16, Supporting Information). Thus, the CPE with the 3D ANF frameworks was beneficial in inhibiting dendrite growth and achieving smooth Li plating and stripping.

2.5. Solid-State Metallic Lithium Battery Performance

All-solid-state lithium metal batteries were assembled with $LiFePO_4$ (LFP) and high-voltage $LiNi_{0.5}Co_{0.2}Mn_{0.3}O_2$ (NCM523) cathodes to evaluate the practical feasibility of the CPE membranes at ambient temperature. The cyclic voltammograms of the Li||LFP cells with different electrolytes at 0.1 mV s^{-1} are shown in Figure S17 (Supporting Information). The Li||LFP cell with the CPE exhibited considerable peak areas and excellent reproductivity, in contrast to those of the PEO-based electrolyte and the SN-LiTFSI/glass fiber composite electrolyte. The higher peak currents of the Li|CPE|LFP cell also suggested a more rapid electrochemical reaction in the cells. As shown in **Figure 5**a, the Li|CPE|LFP cell presented discharge capacities of 161.1, 161.1, 156.6, 154.9, 147.1, and 131.6 mAh g^{-1} at 0.1, 0.2, 0.3, 0.5, 1.0 and 2.0 C, respectively. When the current density returned to 0.2 C, the discharge capacity of the Li|CPE|LFP cell recovered to 159.3 mAh g^{-1}, implying that the Li|CPE|LFP cell had better reversibility and rate performance. However, the Li|PEO|LFP cell displayed worse rate performance with a lower capacity of 101.5 mAh g^{-1} at 0.5 C. The Li|Glass fiber|LFP cell delivered poor rate performance with a low capacity of 0.5 mAh g^{-1} at 2.0 C (Figure S18d, Supporting Information). Meanwhile, the Li|CPE|LFP cell exhibited much lower polarization overpotentials than the Li|PEO|LFP cell and Li|Glass fiber|LFP cell with the increase of the current density (Figure S18a–c, Supporting Information), again confirming that there was no severe side reaction during the continuous cycling process.

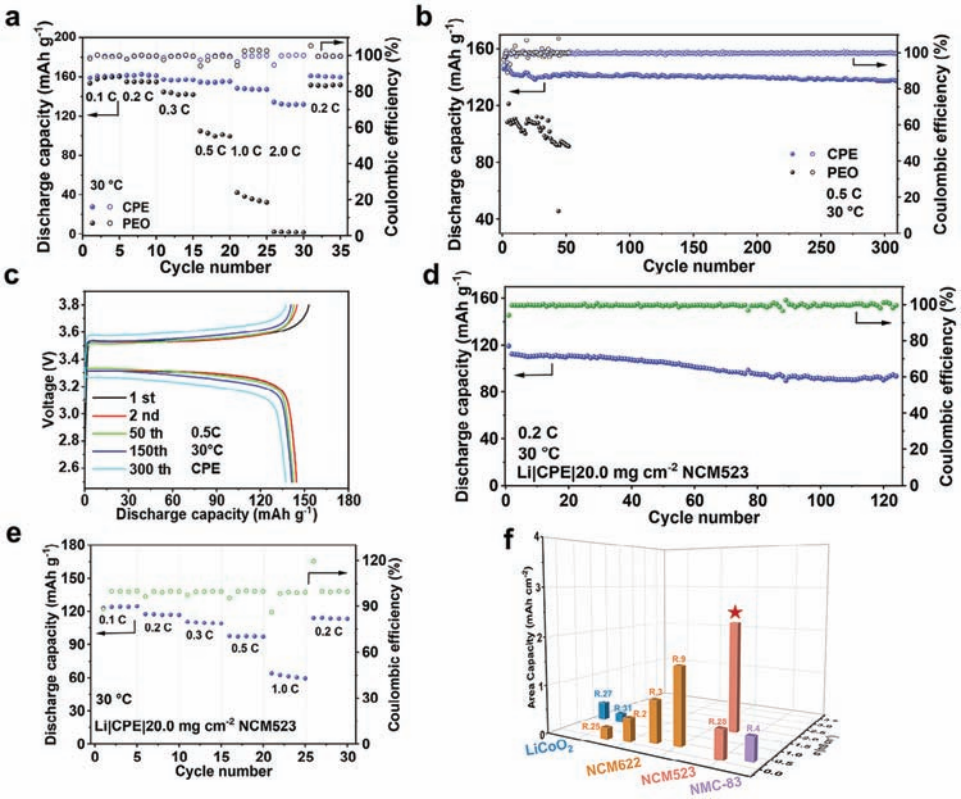

Figure 5. Electrochemical performances of all-solid-state Li-metal batteries at 30 °C. a) Rate performance and b) cycling performance of the solid-state Li||LFP cells. c) Typical charge-discharge profiles of the solid-state Li|CPE |LFP cell at various current densities. d) Cycling performance and e) rate performance of the solid-state Li|CPE|NCM523 cells. f) The comparison of the ionic conductivity and the area capacity of the solid-state batteries (see details in Table S4, Supporting Information).

The long-term cycling performance is shown in Figure 5b. The Li|CPE|LFP cell exhibited an initial discharge capacity of 148.4 mAh g^{-1} at 0.5 C and 30 °C. And the Li|CPE|LFP cell showed a high discharge capacity of 144.6 mAh g^{-1} and a high capacity retention of 94.3% after 300 cycles. In comparison, the Li|PEO|LFP cell exhibited a low initial discharge capacity of 110.2 mAh g^{-1}, and the cell suffered from rapid capacity decay within 55 cycles. The capacity of the Li|Glass fiber|LFP cell also degraded quickly within 70 cycles from 143.2 to 120.1 mAh g^{-1} (Figure S19, Supporting Information). In addition, the charge-discharge curves of the Li|CPE|LFP cell were smooth and the overpotential was almost unchanged (Figure 5c). Furthermore, with the extension of time, the CPE-based cell remained at a lower impedance without a significant increase than the PEO-based cell (Figure S20, Supporting Information). These results verified the application effectiveness of the CPE in ambient-temperature solid-state lithium metal batteries.

Based on the wide electrochemical stability window and high ionic conductivity of the CPE, the loading on the cathode materials in the Li||NCM523 cells was increased to 20 mg cm^{-2} to further examine their practical application. As shown in Figure 5e, the Li|CPE|NCM523 cell presented a decent rate performance. The discharge capacities were 124.5, 116.7, 109.1, 97.5, and 60.4 mAh g^{-1} at 0.1, 0.2, 0.3, 0.5, and 1.0 C, respectively. Once the rate was restored to 0.2 C, the capacity quickly returned to 114.3 mAh g^{-1}. Additionally, the smooth charge/discharge profiles illustrated that no side reactions occurred when charged up to 4.2 V (Figure S21, Supporting Information). The long-term cycling performance of the Li||NCM523 cells at 0.2 C within 2.8–4.2 V is shown in Figure 5d and Figure S22 (Supporting Information). Both the Li|Glass fiber|NCM523 cell and Li|PEO|NCM523 cell displayed poor cycle performance. The Li|PEO|NCM523 cell delivered a lower initial specific capacity of 23 mAh g^{-1} at 0.1 C, and then the capacity decreased to 0.3 mAh g^{-1} at 0.2 C. The Li|Glass fiber|NCM523 cell only showed 65 mAh g^{-1} at 0.2 C after 25 cycles. However, the CPE-based cell showed an initial discharge capacity of 119.1 mAh g^{-1} at 0.1 C after the first activation process, and the corresponding area capacity was as high as 2.14 mAh cm^{-2}. After ultralong 120 cycles at 0.2 C, the cell also delivered a high specific capacity of 111.6 mAh g^{-1} with a capacity retention of 85%. Meanwhile, the potential of the high-loading Li||NCM523 cell was relatively stable over the cycling (Figure S23, Supporting Information). We also compared the area capacity with previous reports and found that our work outperforms other solid-state batteries, as far as we know (Figure 5f; Table S4, Supporting Information). The gravimetric and volumetric energy density of Li|CPE|NCM523 cells were calculated to be 206.3 Wh kg^{-1} and 728 Wh L^{-1}, respectively (Tables S5, and S6, Supporting Information). These results further demonstrated the potential application of the CPE in high-voltage and high-energy-density solid-state lithium metal batteries.

3. Conclusion

In this work, a thin yet ultrahigh ionic conductivity composite electrolyte membrane is obtained by filling SN-LiTFSI matrices in 3D porous ANF frameworks with multiple functions. This polar framework structure of the CPE membranes offers the additional lithium-ion transport pathway along the amide groups and immobilizes the $TFSI^-$ anions, resulting in the high ionic conductivity of 1.69×10^{-3} S cm^{-1} and high Li^+ transference number of 0.57 at 30 °C. In addition, the hydrogen bonding interaction between the –NH groups of the ANFs and the cyano groups of SN can capture the free SN molecules and inhibit the parasitic reactions between SN and lithium metal. Benefiting from these merits, the Li||LFP cell stably cycles over 300 cycles under 0.5 C at room temperature. Further, the high-voltage Li|CPE|NCM523 battery with an ultrahigh active mass loading of 20 mg cm^{-2} delivers a high area capacity with a high capacity retention of 85% after 120 cycles. This work provides a facile yet important route to achieve ultrahigh-ionic-conductivity electrolyte membranes with 3D multifunctional nanofiber frameworks toward ambient-temperature solid-state metallic lithium batteries.

Supporting Information

Supporting Information is available from the Wiley Online Library or from the author.

Acknowledgements

This work is supported partially by the project of National Natural Science Foundation of China (52272200, 52102203, 52302250), Hebei Natural Science Foundation (E2022502022), Beijing Science and Technology Project (Z211100004621010), State Key Laboratory of Alternate Electrical Power System with Renewable Energy Sources (LAPS21004), Huaneng Group Headquarters Science and Technology Project (HNKJ20-H88), 2022 Strategic Research Key Project of Science and Technology Commission of the Ministry of Education, China Postdoctoral Science Foundation (2022M721129), the Fundamental Research Funds for the Central Universities (2022MS030, 2021MS028, 2020MS028), and the NCEPU "Double First-Class" Program.

Conflict of Interest

The authors declare no conflict of interest.

Data Availability Statement

The data that support the findings of this study are available from the corresponding author upon reasonable request.

Keywords

aramid nanofiber framework, composite electrolyte membrane, ionic conductivity, solid-state lithium metal battery

Received: August 11, 2024
Revised: October 2, 2024
Published online:

[1] Y. Lu, C.-Z. Zhao, J.-Q. Huang, Q. Zhang, *Joule.* **2022**, *6*, 1172.
[2] S. Wang, Q. Sun, Q. Zhang, C. Li, C. Xu, Y. Ma, X. Shi, H. Zhang, D. Song, L. Zhang, *Adv. Energy Mater.* **2023**, *13*, 2204036.
[3] J. Sun, C. He, X. Yao, A. Song, Y. Li, Q. Zhang, C. Hou, Q. Shi, H. Wang, *Adv. Funct. Mater.* **2021**, *31*, 2006381.
[4] J. Han, M. J. Lee, K. Lee, Y. J. Lee, S. H. Kwon, J. H. Min, E. Lee, W. Lee, S. W. Lee, B. J. Kim, *Adv. Mater.* **2022**, *35*, 2205194.
[5] Z. Yu, S. Seo, J. Song, Z. Zhang, S. T. Oyakhire, Y. Wang, R. Xu, H. Gong, S. Zhang, Y. Zheng, Y. Tsao, L. Mondonico, E. G. Lomeli, X. Wang, W. Kim, K. Ryu, Z. Bao, *Adv. Energy Mater.* **2022**, *12*, 2201025.
[6] X. Lin, G. Zhou, J. Liu, J. Yu, M. B. Effat, J. Wu, F. Ciucci, *Adv. Energy Mater.* **2020**, *10*, 2001235.
[7] Z. Jiang, S. Wang, X. Chen, W. Yang, X. Yao, X. C. Hu, Q. Han, H. Wang, *Adv. Mater.* **2020**, *32*, 1906221.
[8] W. Chen, H. Duan, J. Shi, Y. Qian, J. Wan, X. Zhang, H. Sheng, B. Guan, R. Wen, Y. X. Yin, S. Xin, Y. G. Guo, L. J. Wan, *J. Am. Chem. Soc.* **2021**, *143*, 5717.
[9] F. Fu, Y. Liu, C. Sun, L. N. Cong, Y. L. Liu, L. Q. Sun, H. M. Xie, *Energy Environ. Mater.* **2022**, *6*, e12367.
[10] G. Liu, J. Shi, M. Zhu, W. Weng, L. Shen, J. Yang, X. Yao, *Energy Storage Mater.* **2021**, *38*, 249.
[11] J. Su, M. Pasta, Z. Ning, X. Gao, P. G. Bruce, C. R. M. Grovenor, *Energy Environ. Sci.* **2023**, *16*, 698.
[12] J. Gao, Q. Shao, J. Chen, *J. Energy Chem.* **2020**, *46*, 237.
[13] J. Wan, J. Xie, X. Kong, Z. Liu, K. Liu, F. Shi, A. Pei, H. Chen, W. Chen, J. Chen, X. K. Zhang, L. Q. Zong, J. Y. Wang, L. Q. Chen, J. Qin, Y. Cui, *Nat. Nanotechnol.* **2019**, *14*, 705.
[14] M. H. Zhou, R. L. Liu, D. Y. Jia, Y. Cui, Q. T. Liu, S. H. Liu, D. C. Wu, *Adv. Mater.* **2021**, *33*, 2100943.
[15] Z. Wang, L. Shen, S. Deng, P. Cui, X. Yao, *Adv. Mater.* **2021**, *33*, 2100353.
[16] L. Yang, D. Luo, Y. Zheng, T. Yang, Q. Ma, Y. Nie, H. Dou, Y. Zhang, R. Huang, A. Yu, L. Shui, X. Wang, Z. Chen, *Adv. Funct. Mater.* **2022**, *32*, 2204778.
[17] S. Xia, B. Yang, H. Zhang, J. Yang, W. Liu, S. Zheng, *Adv. Funct. Mater.* **2021**, *31*, 2101168.
[18] J. M. Whiteley, P. Taynton, W. Zhang, S. H. Lee, *Adv. Mater.* **2015**, *27*, 6922.
[19] R. Y. Li, H. M. Hua, Y. J. Zeng, J. Yang, Z. Q. Chen, P. Zhang, J. B. Zhao, *J. Energy Chem.* **2022**, *64*, 395.
[20] P.-J. Alarco, Y. Abu-Lebdeh, A. Abouimrane, M. Armand, *Nature Mater.* **2004**, *3*, 476.
[21] K. H. Choi, S. J. Cho, S. H. Kim, Y. H. Kwon, J. Y. Kim, S. Y. Lee, *Adv. Funct. Mater.* **2014**, *24*, 44.
[22] D. G. Mackanic, W. Michaels, M. Lee, D. Feng, J. Lopez, J. Qin, Y. Cui, Z. Bao, *Adv. Energy Mater.* **2018**, *8*, 1800703.
[23] J. Pan, Y. Zhang, J. Wang, Z. Bai, R. Cao, N. Wang, S. Dou, F. Huang, *Adv. Mater.* **2022**, *34*, 2107183.
[24] H. Wu, B. Tang, X. F. Du, J. J. Zhang, X. R. Yu, Y. T. Wang, J. Ma, Q. Zhou, J. W. Zhao, S. M. Dong, G. J. Xu, J. N. Zhang, H. Xu, G. L. Cui, L. Q. Chen, *Adv. Sci.* **2020**, *7*, 2003370.
[25] W. Zha, J. Li, W. Li, C. Sun, Z. Wen, *Chem. Eng. J.* **2021**, *406*, 126754.
[26] A. X. Wang, S. X. Geng, Z. F. Zhao, Z. L. Hu, J. Y. Luo, *Adv. Funct. Mater.* **2022**, *32*, 2201861.
[27] T. L. Jiang, P. G. He, G. X. Wang, Y. Shen, C. W. Nan, L. Z. Fan, *Adv. Energy Mater.* **2020**, *10*, 1903376.
[28] C. Li, H. Yue, Q. Wang, J. Li, J. Zhang, H. Dong, Y. Yin, S. Yang, *Solid State Ionics.* **2018**, *321*, 8.
[29] M. J. Lee, J. Han, K. Lee, Y. J. Lee, B. G. Kim, K.-N. Jung, B. J. Kim, S. W. Lee, *Nature.* **2022**, *601*, 217.
[30] C. Wang, H. Zhang, S. Dong, Z. Hu, R. Hu, Z. Guo, T. Wang, G. Cui, L. Chen, *Chem. Mater.* **2020**, *32*, 9167.

[31] L. Liu, J. Lyu, J. Mo, H. Yan, L. Xu, P. Peng, J. Li, B. Jiang, L. Chu, M. Li, *Nano Energy.* **2020**, *69*, 104398.
[32] F. Wu, Z. He, L. Liu, S. Guan, F. Wang, Y. Huang, *Chem. Eng. J.* **2023**, *471*, 144477.
[33] B. Yang, L. Wang, M. Y. Zhang, J. J. Luo, Z. Q. Lu, X. Y. Ding, *Adv. Funct. Mater.* **2020**, *30*, 2000186.
[34] C. J. Xie, S. Y. Liu, Q. G. Zhang, H. X. Ma, S. X. Yang, Z. X. Guo, T. Qu, X. L. Tuo, *ACS Nano.* **2021**, *15*, 10000.
[35] P. Y. Hu, J. Lyu, C. Fu, W. B. Gong, J. H. Liao, W. B. Lu, Y. P. Chen, X. T. Zhang, *ACS Nano.* **2020**, *14*, 688.
[36] Q. Liu, Q. Yu, S. Li, S. Wang, L. Zhang, B. Cai, D. Zhou, B. Li, *Energy Storage Mater.* **2020**, *25*, 613.
[37] M. Zuo, Z. Bi, X. Guo, *Chem. Eng. J.* **2023**, *463*, 142463.
[38] M. Liao, Y. Zhou, X. Jiang, R. Wan, *Chem. Eng. J.* **2024**, *480*, 148020.
[39] M. M. Zhang, P. Pan, Z. L. Cheng, J. T. Mao, L. Y. Jiang, C. K. Ni, S. K. Park, K. Y. Deng, Y. Hu, K. K. Fu, *Nano Lett.* **2021**, *21*, 7070.
[40] Z. Ren, J. Li, Y. Gong, C. Shi, J. Liang, Y. Li, C. He, Q. Zhang, X. Ren, *Energy Storage Mater.* **2022**, *51*, 130.
[41] L. Gao, S. B. Luo, J. X. Li, B. W. Cheng, W. M. Kang, N. P. Deng, *Energy Storage Mater.* **2021**, *43*, 266.
[42] F. He, W. Tang, X. Zhang, L. Deng, J. Luo, *Adv. Mater.* **2021**, *33*, 2105329.
[43] W. Liu, G. Li, W. Yu, L. Gao, D. Shi, J. Ju, N. Deng, W. Kang, *Energy Storage Mater.* **2023**, *63*, 103005.
[44] F. Wang, Y. Wu, Y. Huang, L. Liu, *Compos. Sci. Technol.* **2018**, *156*, 269.
[45] A. M. Hindeleh, S. M. Abdo, *Polymer.* **1989**, *30*, 218.
[46] Y. Ye, X. Zhu, N. Meng, F. Lian, *Adv.Funct.Mater.* **2023**, *33*, 2307045.
[47] Y. Jin, R. Lin, Y. Li, X. Zhang, S. Tan, Y. Shuai, Y. Xiong, *Angew. Chem., Int. Ed.* **2024**, *63*, e202403661.
[48] Q. Wu, M. Fang, S. Jiao, S. Li, S. Zhang, Z. Shen, S. Mao, J. Mao, J. Zhang, Y. Tan, K. Shen, J. Lv, W. Hu, Y. He, Y. Lu, *Nature Commun.* **2023**, *14*, 6296.
[49] Y. Cheng, X. Liu, Y. Guo, G. Dong, X. Hu, H. Zhang, X. Xiao, Q. Liu, L. Xu, L. Mai, *Adv. Mater.* **2023**, *35*, 2303226.
[50] J. Hu, C. Lai, K. Chen, Q. Wu, Y. Gu, C. Wu, C. Li, *Nat. Commun.* **2022**, *13*, 7914.
[51] X. Lan, S. Yang, T. Meng, C. Zhang, X. Hu, *Adv. Energy Mater.* **2023**, *13*, 2203449.
[52] R. Xu, C. Yan, Y. Xiao, M. Zhao, H. Yuan, J. Q. Huang, *Energy Storage Mater.* **2020**, *28*, 401.